Contributions of morphological and structural parameters at different hierarchical morphology levels to photocatalytic activity of mesoporous nanostructured ZnO

Citation

SEDLÁK, Jakub, Ivo KUŘITKA, Milan MASAŘ, Michal MACHOVSKÝ, Pavel URBÁNEK, Pavel BAŽANT, Pavel JANOTA, and Marie DVOŘÁČKOVÁ. Contributions of morphological and structural parameters at different hierarchical morphology levels to photocatalytic activity of mesoporous nanostructured ZnO. *Applied Surface Science* [online]. vol. 513, Elsevier, 2020, [cit. 2023-02-02]. ISSN 0169-4332. Available at https://www.sciencedirect.com/science/article/pii/S0169433220305298

DOI

https://doi.org/10.1016/j.apsusc.2020.145773

Permanent link

https://publikace.k.utb.cz/handle/10563/1009601

Contributions of morphological and structural parameters at different hierarchical morphology levels to photocatalytic activity of mesoporous nanostructured ZnO

Jakub Sedlak[a], **Ivo Kuritka**[a,*], **Milan Masar**[a], **Michal Machovsky**[a], **Pavel Urbanek**[a], **Pavel Bazant**[a], **Pavel Janota**[b], **Marie Dvorackova**[b]

[a]*Centre of Polymer Systems, University Institute, Tomas Bata University in Zlin, tr. Tomase Bati 5678, 760 01 Zlin, Czech Republic*

[b]*Department of Environmental Protection Engineering, Faculty of Technology, Tomas Bata University in Zlin, Vavreckova 275, 760 01 Zlin, Czech Republic*

* *Corresponding author. E-mail addresses: kubasedlak@gmail.com (J. Sedlak), kuritka@utb.cz (I. Kuritka), masar@utb.cz (M. Masar), machovsky@utb.cz (M. Machovsky), urbanek@utb.cz (P. Urbanek), bazant@utb.cz (P. Bazant), pave.janota@gmail.cz (P. Janota), dvorackova@utb.cz (M. Dvorackova).*

ABSTRACT

Hierarchical mesoporous zinc oxide (ZnO) polyhedral micro-lumps were prepared by annealing zinc oxalate dihydrate ($ZnC_2O_4 \cdot 2H_2O$) precursor in an air atmosphere at various temperatures. The development of the mesoporous nanoarchitecture of the ZnO micro-lumps was studied by XRD analysis corroborated with the analysis of their specific surface area utilizing nitrogen sorption via BET method. Investigations by high-resolution SEM revealed a morphology resembling calcined mesocrystals. A description of the sintering process and the crystallite growth is given together with an analysis of the activation energy of the grain and crystallite growth, respectively. The self-diffusion coefficient, diffusion mechanisms, and its activation energy involved in the growth of crystallites were identified. The crystallite size and the specific surface area can be tuned by varying the annealing temperature, while the UV-vis and PL spectra remain nearly unchanged. The morphological and structural parameters are correlated with photocatalytic activity evaluated by the UV discolouration of the Methyl violet 2B. An interpretational framework, including three hierarchical morphology levels of the micro-lumps, was developed. The interplay between the contributions of the different promoting and impeding effects emerging on various levels can explain the non-monotonous dependence of the photocatalytic activity on the catalyst annealing temperature.

Keywords: Hierarchical, photocatalysis, ZnO, mesoporous, self-diffusion coefficient, grain growth

1. Introduction

For a long time, zinc oxide (ZnO) has drawn serious attention from the scientific community as a versatile semi-conductive material with a direct wide band gap of approximately 3.37 eV and a large exciton binding energy of about 60 meV in bulk at room temperature. It can be easily doped by both the p- and n-type dopants. Its band gap can be engineered to the desired value by a simple substitution of Zn for other divalent ions [**1,2**]. These characteristics make ZnO a promising material in the field of electronics, solar cells, light-emitting devices, gas sensors, and photocatalysis [**3-8**]. Moreover, ZnO can be prepared by various chemical or physical methods in different shapes. Thus, a plethora of morphology-dependent properties can be obtained such as, thin films, quantum dots, nanorods, nanowires, nanosheets, as well as complex shape structures assembled from low-dimensional crystal components [**9-12**].

Many useful properties of ZnO are related to a high surface area to the volume ratio. Among them, catalysis and photocatalysis critically depend on a specific surface area, besides other factors. Therefore the use of nano-ZnO is the first choice for photocatalysis [**13**]. However, the issues of safety and risk management occur when dealing with nanomaterials, although their micro-sized analogues are considered green and non-toxic. The eventual toxicity of nano-sized ZnO and the inconvenience of removing the catalyst from the reaction system hamper the wider use of such materials [**14**]. Therefore, it seems to be reasonable to prepare materials with nanostructured building blocks packed safely into a micro-scale sized body. This concept of hierarchically organised multiscale materials was successfully introduced in medical plastics in our previous work [**15**]. Classic bottom-up strategies are usually quite demanding on chemicals and processing complexity. Their counterparts, i.e., top-to-bottom techniques are elementary, but they give primitive forms of products suffering from non-uniformity and defects [**16**]. A combination of these two approaches seems to be a suitable method. Two-dimensional, as well as three-dimensional porous nanostructured materials, have been successfully demonstrated [**17,18**].

So-called hierarchical photocatalysts have received significant scientific interest as promising solution for improving the overall efficiency of the photocatalytic process. An ideally designed hierarchical structure of a photocatalyst can not only enhance specific surface area and the concentration of active sites but also increase light-harvesting and improve diffusion mass transfer of the substrate molecules, intermediates and products of the degradation [**19-21**].

Although specific surface area and crystallinity of photocatalysts are generally considered to be most prominent [**22,23**], many studies showed a much more complex behaviour for hierarchical structures [**24-31**]. Light in-coupling can be improved by the presence of macropores or cavities of comparable dimension to the wavelength of the incident photons by multiple scattering inside the material [**21**]. The porous architecture of the catalyst integrating multiple levels of porosity on the length scale from micro-, meso- to macropores influences transport of the substrate molecules to the active surface sites as well as transport of reactive species and products released by the reactions out of the active surface [**20**]. Finally, the material structure influences the overall photocatalytic efficiency by the cumulative effects of several variables, namely on the light absorption efficiency, charge excitation/ separation efficiency, charge migration, transport efficiency, and charge utilization efficiency for the catalytic reaction [**22,24-31**].

Here we present a study on a model photocatalyst material with hierarchical morphology. Zinc oxalate dihydrate was chosen as the best possible candidate for the preparation of a nanostructured high specific surface area mesoporous microsized ZnO lumps [**32-36**]. The annealing temperature influenced the structural properties and morphology of ZnO micro-lumps at three hierarchical scale levels ranging from individual nanocrystallites through their assemblies in grains up to the lumps morphology at a micrometre length. The annealing process was analysed with unprecedented complexity and detail up to the identification of the diffusion mechanisms involved in the material formation. Once obtained, the photocatalytic performance of the prepared ZnO nanostructured lumps was evaluated in a standard methyl violet UV discolouration test [**37,38**] and results correlated with the given morphological and structural properties of the photocatalyst.

2. Material and methods

2.1. Preparing the precursor

Zinc acetate dihydrate, p.a., (Penta, Czech Republic) and oxalic acid dihydrate, p.a., (Penta, Czech Republic), were used as the starting chemicals. The precursor ($ZnC_2O_4 \cdot 2H_2O$) was prepared by simple precipitation of a 400 mL 0.05 M solution of zinc acetate with the addition of a 200 mL of 0.5 M solution of oxalic acid at room temperature under a vigorous agitation of a magnetic stirrer for 5 min. The resulting precipitates were separated by suction filtration, washed several times with distilled water to remove possible by-products or any residues of the original soluble chemicals. The filtration cake was left to dry at 42 °C in a ventilated oven for 24 h.

2.2. Annealing the precursor

The obtained white precursor powder was subjected to thermal heating in a muffle furnace (LMH 07/12, LAC, Czech Republic) up to different temperatures (400 °C; 500 °C; 700 °C and 900 °C). All of these samples were annealed by a constant heating rate of 10 °C/min and then held at the maximum temperature (an isothermal step) for one hour. The heating rate was chosen the same as in the thermogravimetric analysis. Then, the oven was left to cool fast naturally without controlling the cooling rate, and the annealed precursors were removed from the furnace at room temperature.

2.3. Testing photocatalytic aktivity

The photocatalytic activity of the ZnO porous powders was evaluated by measuring the photocatalytic discolouration of the Methyl Violet 2B (MV) in distilled water under the constant illumination of a 100 W focused UV-lamp (Super-Light C 10 A-SH, Helling Gmbh., Germany) with the strongest emission at 365 nm. The temperature of the reaction mixture was maintained at approx. 25 °C by thermostatic circulation through the double-wall glass beaker. In a typical experiment, 50 mg of the ZnO porous powder sample was added into the double-wall glass beaker containing 50 mL of MV solution, having a concentration of 3.7 mg/L. The concentration was set intentionally low to start the experiment from the absorbance value of about 0.2 and to achieve complete (or nearly complete) discolouration of the solution within reasonable experimental time (2 h). Before the start of the discolouration experiment, the suspension was stirred in the dark for at least 10 min to assure a complete adsorption/desorption equilibrium of used dye on the surface of the ZnO particles. During the experiment, 12 samples of the solution with a volume of 1 mL were taken from the reaction suspension within a time range of 0 to 120 min and filtered through a syringe filter to remove the ZnO catalyst from the solution. The time-dependent discolouration was monitored by measuring the absorption of the MV solutions at 580 nm by UV-vis spectroscopy [**18**].

The role of active species in the discolouration process was also investigated. Ethylenediaminetetraacetic acid (EDTA) and tert-butanol were added to the suspension as specific scavengers for holes (h^+) and hydroxyl radicals (OH), respectively [**39-41**].

2.4. Characterization techniques

The TA Q 500 apparatus (TA Instruments, US) was used for the thermogravimetric analysis (TGA). This analysis was performed at a constant heating rate of 10 °C/min within a stable airflow. The amount of each sample was approximately 15 mg.

Microscopic images of the samples were taken using the scanning electron microscope Nova NanoSEM 450 (FEI company, ThermoFischer Scientific, The Czech Republic) at accelerating voltage 5 kV. The eucentric working distance was 5 mm.

The UV-Vis diffuse reflectance of prepared powders was studied with the UV-Vis spectrometer AvaSpec 2048-2 with the light source AvaLight-DHS-DUV equipped with an integrating sphere ($BaSO_4$ coated) and white tile $BaSO_4$ reflectance standard (Avantes, The Netherlands).

Room temperature photoluminescence (PL) emission spectra were measured for all annealed samples by the FLS 920 Fluorescence spectrometer (Edinburgh Instruments, The United Kingdom). A solid-state laser at λ_{exc} = 332.2 nm was used for excitation.

The crystalline phase structure of the prepared powders was characterized by powder X-ray diffraction (XRD) using the XPert PRO X-ray diffractometer (PANalytical, The Netherlands) with a Cu Kα radiation of λ = 0.15406 nm. The size of the ZnO nanocrystallites was considered to be nearly identical to the size of the diffracting area d_{diffr} which is easily accessible via Scherrer's formula using $\Delta(2\theta)$ which is full-width at half-maximum (FWHM) of the line in the XRD patterns. The particle shape and other factors were neglected to simplify the procedure, and the calculation followed this well-known formula [**42**]:

$$d_{diffr} = \frac{0.9\lambda}{\beta \quad cos\theta} \tag{1}$$

In which the constant 0.9 is the shape factor, λ is the wavelength of the X-ray source, β is the FWMH in the radians [**43**]. The actual value of β was obtained by a deconvolution of the instrumental broadening effects using the Warren correction method. The θ is the Bragg angle, i.e., half of the 2θ position, of the selected diffraction line. Since a non-monochromatised X-ray source was used, a doublet of Lorentzian peaks was fitted to the corresponding peaks of the diffractogram to estimate the broadening. Coarse ZnO standard powder was used to obtain instrumental function.

The specific surface area A_{BET} was obtained via a multipoint Brunauer-Emmet-Teller analysis of the nitrogen adsorption/desorption isotherms at 77 K recorded by the Belsorp-mini II (BEL Japan, Inc.) apparatus. The grain size is expressed as the mean diameter d_{BET}, according to reference [**44**]:

$$d_{BET} = \frac{6}{\rho_{S\text{-}A_{BET}}} \tag{2}$$

In which the p_s is a density of the adsorbent material.

The study of the UV-Vis absorption of the solutions was performed with the aid of the UV-Vis spectrometer (UV-Vis Varian Cary 300, Varian Inc., United States). The absorbance was recorded for wavelengths in a range of 300-800 nm. The data were evaluated by fitting the pseudo-first-order kinetic model.

The data processing, the graph plotting, and the fitting by models were performed in the Origin 2016 software. The obtained constants for each dataset were rounded up according to the standard error calculated by the data fitting procedure also in the Origin software. The standard error is given when available and indicated by the ± symbol. The data in **Table 1**, which are related to the XRD and BET experiments, were obtained by single measurements for each sample. However, a series of samples was investigated. Our estimate of data error is indicated by rounding the values up to three significant figures. Although it may seem exaggerated, it is in accord with the nearly perfect correlation of the data.

3. Results and discussions

3.1. Preparing the ZnO nanostructured micro-lumps and their characteristics

The composition of the prepared zinc oxalate dihydrate was analysed by the thermogravimetric analysis (TGA) in an air atmosphere. The thermogravimetric curve, as well as the mass-loss rate obtained as its derivative, is plotted in **Fig. 1**. The decomposition occurs in two steps. The first is a mass loss of approx. 18% and corresponds to the loss of crystal water. The second step connected with a loss of 39% of the sample mass is attributed to the oxidative decomposition of anhydrous zinc oxalate into the ZnO, carbon dioxide, and water. The mass-loss rate reaches its maximum at 390 °C, as evident from the -dTG curve. The decomposition reactions can be summarised as follows:

$$\mathrm{ZnC_2O_4 \cdot 2H_2O \rightarrow ZnC_2O_4 + 2H_2O} \qquad (3)$$

$$\mathrm{ZnC_2O_4 + 1/2O_2 \rightarrow ZnO + 2CO_2} \qquad (4)$$

These results are in good agreement with previous studies and the composition derived from the structural formula [**45,46**]. During the thermal decomposition process, the $ZnC_2O_4 \cdot 2H_2O$ precursor undergoes dehydration and decomposition, which is accompanied by an evolution of gaseous reaction products. These processes lead to the formation of a high-density porous structure in the material. Because ZnO nucleates and grows uniformly in particles of the precursor, the obtained ZnO lumps keep the same overall morphology retaining the shape of the original crystals of the precursor [**18**].

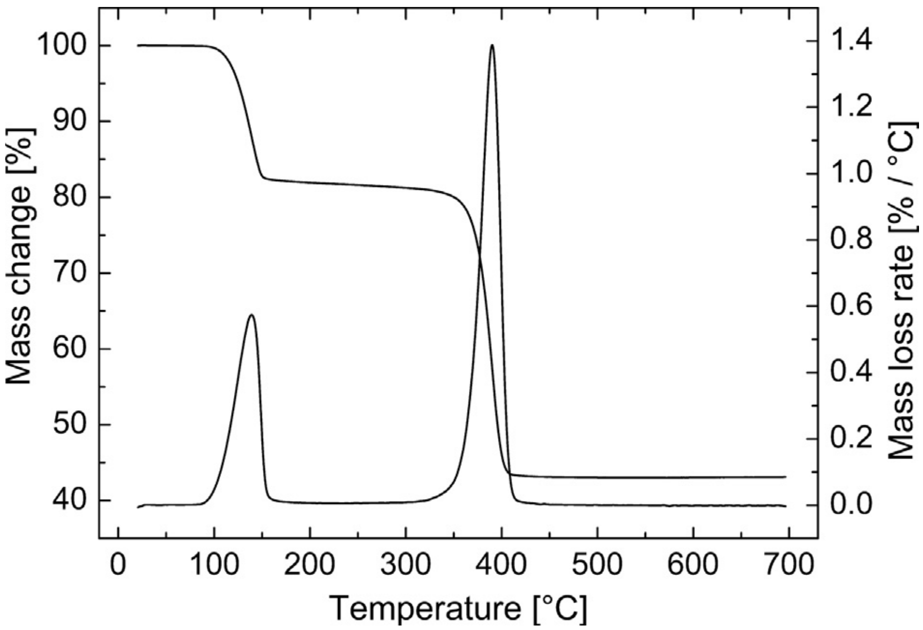

Fig. 1. The TGA analysis of the precursor in an air atmosphere.

The initial pores in the precursor are formed by the release of crystal water molecules (see Eq. (**3**)), which may be the main reason that the calcined product can preserve its precursor morphology [**47**]. However, the second decomposition step has a more complicated mechanism than summarised in Eq. (**4**) in the previous paragraph. The oxalate decomposes into solid zinc oxide and releases carbon dioxide and carbon monoxide (see Eq. (**5**)) which is subsequently oxidised in the gaseous phase by oxygen from the air atmosphere (see Eq. (**6**)) [**48**].

The initial pore structure development caused by dehydration is followed by a second stage during which the pore volume increases further with the release of CO_2 and CO, which proceeds simultaneously with the nucleation and growth of the ZnO primary nanoparticles. Hence, the oxygen delivered from the ambient air atmosphere is not a necessity for the ZnO formation yet oxygen-rich atmosphere may avoid the development of oxygen vacancies [**48-51**].

As seen in **Fig. 1**, the second decomposition step finishes approximately at a temperature of 400 °C if the heating rate is 10 °C/min. Therefore, the first temperature for the series of the annealing experiment was set to 400 °C.

The precursor was obtained in the form of polyhedral crystals ranging in size, mainly from 1 to 3 µm, with only a small portion of less developed particles. No particles smaller than several hundreds of nanometres were observed. The samples obtained by annealing at selected temperatures were analysed by electron microscopy. Their morphology is exemplified in high-resolution SEM images in **Fig. 2**. The product of annealing keeps the overall size and the polyhedral envelope shape of the precursor on a micrometric scale. Thus, the particles are denoted as micro-lumps. It is evident that its surface is fissured into a very dense network of cracks, and the whole particle became a porous yet undisrupted assembly of nanoparticles by the annealing procedure. The morphology strongly resembles typical morphologies obtained for calcined zinc oxalate [**35**] or copper oxalate [**52,53**] mesocrystals.

Table 1 A summary of the XRD and the BET analyses of the annealed samples. The last row contains the rate constant obtained for the photocatalysis reaction.

	annealing temperature	400 °C	500 °C	700 °C	900 °C
XRD met.	crystallite size, d_{diffr} [nm]	21.0	47.1	67.8	79.3
	crystallite surface area, A_{diffr} [m^2g^{-1}]	51.0	22.7	15.8	13.5
BET method	BET surface area, A_{BET} [m^2g^{-1}]	29.9	10.2	3.4	1.7
	BET total pore volume, $V_{p\ BET}$ [$10^{-2}cm^3g^{-1}$]	3.55	1.12	0.36	0.17
	BET mean pore diameter, $d_{p\ BET}$ [nm]	4.7	4.4	4.2	4.0
	grain size, d_{BET} [nm]	36	105	315	630
UV cat.	rate constant, k [s^{-1}]	0.044 ± 0.002	0.066 ± 0.002	0.041 ± 0.002	0.039 ± 0.002

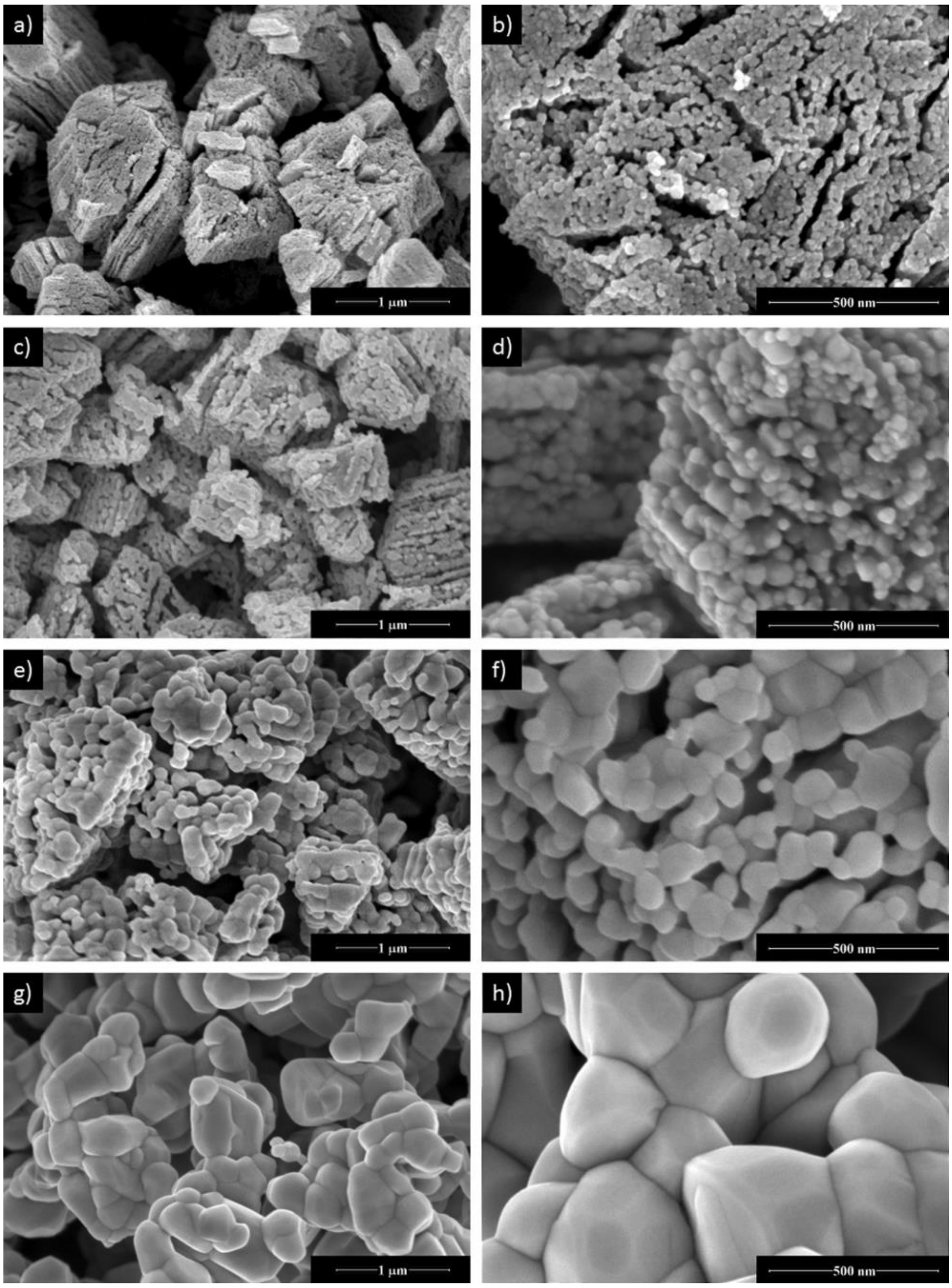

Fig. 2. Low and high magnification FESEM images (left and right column, respectively) of the products prepared by annealing the precursor at different temperatures: (a) and (b) 400 °C; (c) and (d) 500 °C; (e) and (f) 700 °C; (g) and (h) 900 °C.

However, in this presented case, there was no need to build up the mesocrystal from individual nanocrystal bricks with the aid of a polymer agent. With increasing temperatures, the coarsening of the particle structure can be observed. The size of the grains ranges from several tens up to several hundred nm. Sintering and coalescence of the grains can be followed from images directly by the naked eye.

The conversion of the micro-sized inorganic precursor into the final zinc oxide nanostructured lumps can be analysed according to the results of the XRD analysis in **Fig. 3**. Compared with the ICDD PDF-2 entry 25-1029, the diffraction peaks of the precursor match well with those of the monoclinic $ZnC_2O_4 \cdot {}_2H_2O$ and the diffraction peaks of all the annealed products match well with those of a hexagonal ZnO wurtzite structure given in the ICDD PDF-2 entry 01-074-0534. The shape of the diffractogram background testifies for a relatively well-developed crystalline phase and no or negligible presence of an amorphous phase. The ratios between the intensities of the diffraction peaks do not change with an increase in the annealing temperature. Thus, no changes to the aspect ratio and the preferential development of specific crystal faces were observed unlike in the reference [**54**].

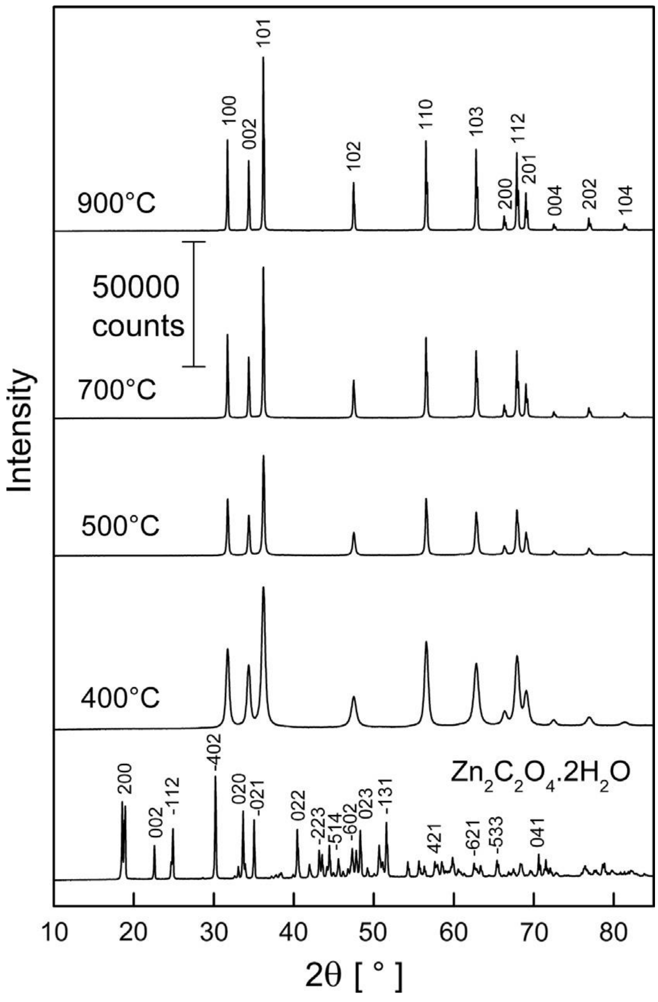

Fig. 3. X-ray powder diffractograms with indexed diffraction lines of the precursor and the ZnO samples obtained by annealing at temperatures indicated in the graph.

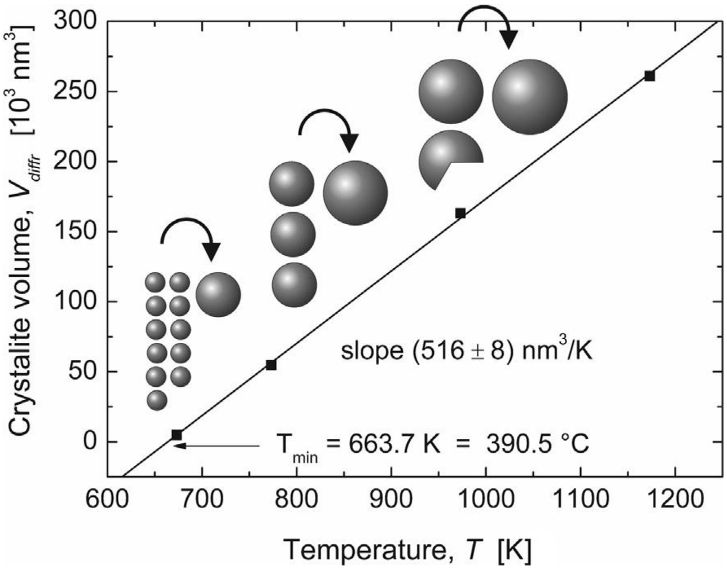

Fig. 4. The calculated crystallite volume of the ZnO samples annealed at different temperatures.

The diffraction line from the (10 1) planes in ZnO that appears in diffractograms at 20 angle 36.2° was used for the diffracting area size calculation. The results are listed in **Table 1** alongside the results of the other analyses discussed below. The diameter of nanocrystallites ($d_{diff.}$) grows with the temperature of annealing. The specific crystallite surface area (A_{diff}) was calculated from the size of crystallites, and the material density of ZnO (5.6 g/cm^3). The volume of crystallites (V_{diff}) was calculated, and the obtained values are shown in **Fig. 4**. The dependence of V_{diff} on the temperature is perfectly linear. This result is not as surprising as it might seem initially. The growth of one crystallite proceeds at the expense of other crystallites, hence the total volume change of the material is zero. The ball diagram inserted into the graph shows how many crystallites of each size are needed to create one bigger crystallite at the next annealing temperature step. The intercept of the linear dependence with the abscissa is the minimum possible temperature at which the crystallite size would be theoretically zero. This initial temperature of ZnO (nano)crystallite formation is 663.7 K (390.5 °C), and it is identical to the maximum second step decomposition rate temperature of the precursor.

A comparison of the results obtained from the X-ray diffraction line broadening analysis with the results obtained from the gas sorption BET analysis is useful. The first and usually the most sought after information from the BET is the Specific surface area (A_{BET}). The obtained values are relatively high and in agreement with other literature values available for similar systems. The values ranging from 30 m^2/g for nano-disperse material up to only several m^2/g for submicrometric powders (compare with the commercial ZnO materials for rubber vulcanisation) can be considered as typically achievable for ZnO nanostructured materials [**51,55**]. At first sight, the A_{BET} is smaller than the specific crystallite surface area. The X-ray diffraction characteristics are correctly obtained for coherently diffracting areas, i.e., to the size of the nanocrystallites (nanocrystalline domains), while the gas sorption analysis examines the actual surface of the porous body accessible to N_2 molecules, which means that it characterises the surface of the grains. Thus, the A_{BET} is related to the surface of the grains, which consist of one or more crystallites and an amorphous phase if the amorphous phase is present at all. The ratio between these two specific areas is called the packing factor (1/F), which gives information on particle aggregation/agglomeration and the availability of the nanocrystallite surface to the adsorption of the molecules [**32,56**]. Fig. 5 shows the dependence of 1/F on the annealing temperature for the prepared materials. The packing factor decreases considerably with increasing temperature.

The total pore volume estimated by the BET analysis V_{pBET} decreases with the annealing temperature similarly as the A_{BET}, while the BET mean pore (diameter) d_{pBET} decreases very slowly from 4.7 to 4.0 nm which classifies these materials as mesoporous (see **Table 1**). Assuming that the grains have a spherical shape and a uniform size, the average particle size can be estimated according to Eq. (**2**) as the grain size (d_{BET}). The obtained values confirm reasonable coarsening of the particles due to sintering with increasing annealing temperature and are evidently in agreement with the SEM observations even without any image analysis. Under the same assumptions concerning the mean values obtained from the XRD and the BET, the ratio between the grain and the crystallite volumes can be calculated. This ratio is plotted in **Fig. 6** and characterises how many ZnO (nano)crystallites aggregate into one grain. The value increases from ca. 5 for 400 °C to ca. 500 for 900 °C. The observed linear dependence of the logarithm of this ratio on the thermodynamic temperature can be extrapolated into the initial temperature (Tmin) and compared with the crystallite volume dependence.

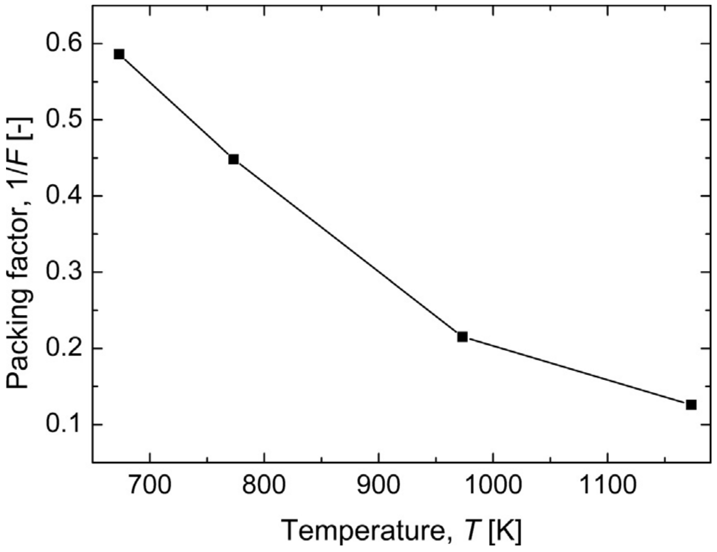

Fig. 5. Plot of the Packing factor (1/F) versus the thermodynamic temperature for the annealed ZnO samples. The solid lines connecting data points are only guides for eyes.

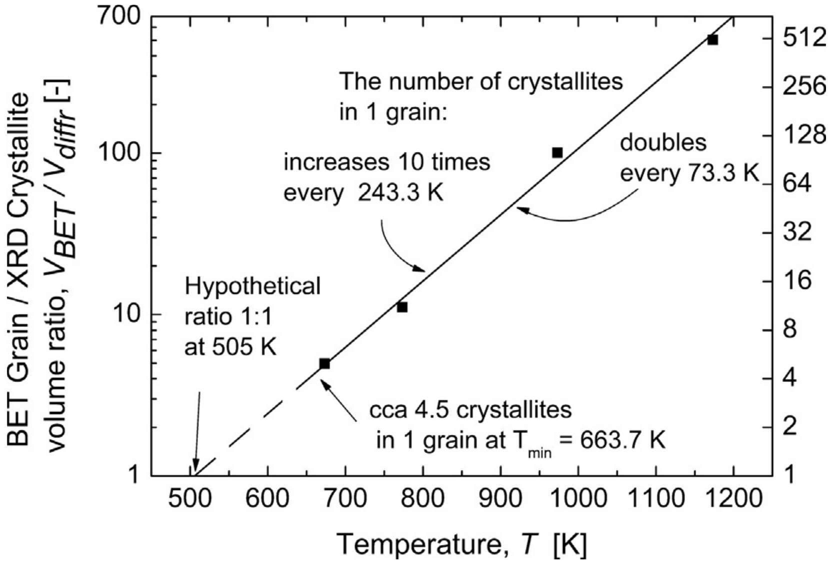

Fig. 6. A semi-log plot of the BET Grain / XRD Crystallite volume ratio versus the thermodynamic temperature for the annealed ZnO samples.

It seems that the first (nano)crystallites already appear in a grain assembly with a mean number of crystallites of about 4.5 per grain. Moreover, the hypothetical 1:1 ratio can be obtained at 505 K (232 °C) by extrapolation, which is deeply below the decomposition temperature of the dehydrated precursor. According to this, it can be deduced that the initial aggregation of a few building blocks occurs most likely as the result of the dehydration process in the first mass loss step.

The annealing of the precursor leads to the sintering of the ZnO nanoparticles. As shown in **Fig. 6**, the number of crystallites sintered into one grain doubles every 73.3 K with an increase in temperature. Activation energy is a characteristic constant of this process. Although various approaches can be used, for the sake of simplicity, the basic models are favoured. A linear relationship between the rate of grain growth and the inverse grain size is assumed, which in turn is proportional to the radius of the curvature of the grain [**57,58**].

$$\frac{\mathrm{d}X}{\mathrm{d}t} = \frac{k}{X} \tag{7}$$

In which X is the length scale, i.e., the diameter of the grain, t is time, and k is the rate constant depending on temperature (T). This equation can be integrated with X0 being the integration constant as the grain size at t =0.

$$X^2 - X_0^2 = k \cdot t \tag{8}$$

Although this equation describes an ideal state and many corrections and improved models have been introduced, it still works well in many cases and is a perfect first choice. The use of the second power is assumed above in specific surface area analysis. Here, this approximation means that the growth of the convex polyhedral shape of grain (as well as crystallites - see below) proceeds in all directions with the same rate as it would be in case of a growing sphere. On the other hand, accepting this, we resign from a more detailed analysis of the shape growth and development that was demonstrated elsewhere [**32**]. The use of empirical power coefficient n could cover larger diversity of shapes [**32**]; however, it generally increases the number of free parameters in the fitting procedure and increases their dependency, especially if the number of experimental data points is low.

The constant k depends exponentially on temperature.

$$k(T) \propto e^{\frac{-Ea}{RT}} \tag{9}$$

In which R is the gas constant (8.314 $\mathrm{Jmol^{-1}K^{-1}}$), and the activation energy (Ea) for the sintering process can be estimated easily from the Arrhenius plot for the values obtained at the same annealing time. In our case, the heating rate of 10 °C/min is considered high enough concerning the isothermal holding time of 1-hour annealing. Under real experimental conditions, it is difficult to estimate the X_0 constant correctly.

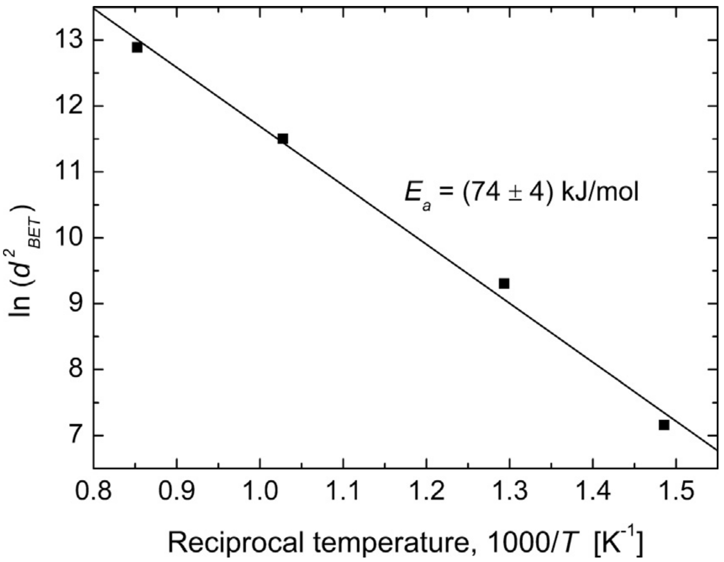

Fig. 7. The activation energy of the sintering of the annealed ZnO obtained from a linear plot of data according to the Eq. (**8**).

The integration constant is a hypothetical grain diameter at the time zero. The zero-time estimation is an 'old pain' in the thermal analysis - see our initial assumptions concerning the heating rate in comparison with the holding time. Nevertheless, the X_0 constant is often relatively small and does not influence the result much in cases of steep dependences. Hence it may be neglected for practical reasons, and the Eq. (**8**) transforms for d_{BET} into:

$$\ln d_{BET}^2 = -\frac{E_{as}}{R}\cdot\frac{1}{T} + const \tag{10}$$

Another approach is to use the value of the grain diameter obtained for the lowest annealing temperature as the initial guess of X_0. Then, the following equation is obtained.

$$\ln(d_{BET}^2 - d_{BET0}^2) = \ln(d_{BET}^2 - d_{BET}^2(400^{\circ}C)) = -\frac{E_{as}}{R}\cdot\frac{1}{T} + const \tag{11}$$

It can be expected that the correct value lies within the interval between the two values obtained by these approaches. The results are plotted in graphs in **Figs. 7 and 8**. Indeed, the activation energy for the corrected data is slightly lower, and the actual value can be found between 74 and 70 kJ/mol.

A similar approach can be adopted for the data obtained from the XRD analysis. However, a linear dependence of $(d_{diff.})^2$ on the reciprocal value of the thermodynamic temperature was found.

Such dependence points towards the crystallite growth rate (u) derived as a product of the Gibbs energy change (ΔG) and crystallite boundary mobility (M).

$$u = \Delta G \cdot M \tag{12}$$

Following our notation, change to the Gibbs energy is proportional to the specific surface energy (ϒ) and the molar volume (V_{mol}). The term in brackets represents a change in the size of the crystallites between the integration limits [**59**].

$$\Delta G = -4\gamma V_{mol}\left(\frac{1}{d_{diffr1}} - \frac{1}{d_{diffr2}}\right) \tag{13}$$

The crystallite boundary mobility (M) is dependent on the self-diffusion coefficient D_s:

$$M = \frac{D_s}{k_B T \lambda} \tag{14}$$

In which k_B is the Boltzman constant, *T* is the thermodynamic temperature, and λ is the thickness of the boundary, usually in the order of the size of the atoms. In general form i.e., without λ, the Eq. (**14**) is known as the Einstein relation.

Thus, we can obtain the rate constant k' from the Eqs. (**12**)-(**14**) and substitute k_B with R due to the use of $V_{mol.}$

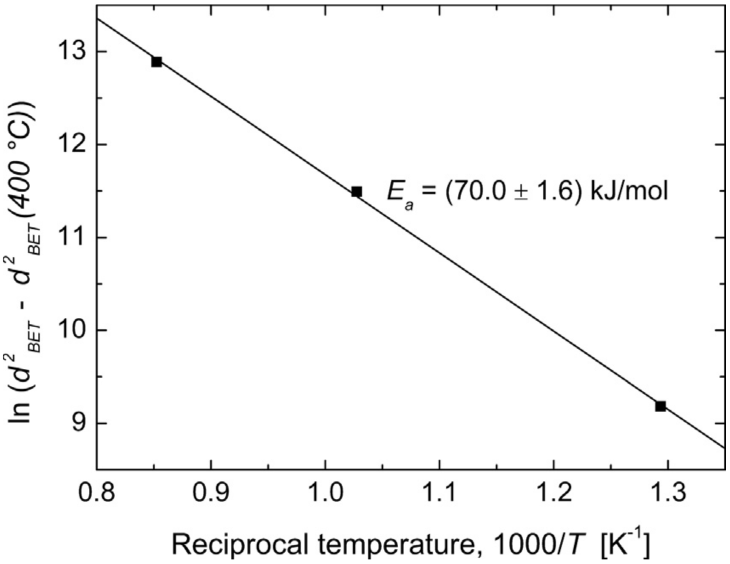

Fig. 8. The activation energy of the sintering of the annealed ZnO obtained from a linear plot of data according to the Eq. (**9**).

$$k' = -\frac{4\gamma D_s V_{mol}}{RT\lambda} \tag{15}$$

Adaption of the Eq. (**8**) yields:

$$d_{diffr}^2 - d_{diffr0}^2 = -k' \cdot t \tag{16}$$

However, we obtained V_{diffr} = 0 nm^3 =>d_{difr} = 0 nm for the lower integration limit (see **Fig. 4**, the minimum temperature 390.3 °C).

Thus the Eq. (**16**) can be formulated as:

$$d_{diffr}^2 = -k' \cdot t \tag{17}$$

It must be noted that this approach considers the surface energy as a constant together with the assumption of the temperature independence of the molar volume. Therefore, the slope of the linear plot in **Fig. 9**, according to the Eq. (**17**), contains contributions from at least two other yet minor terms and did not entirely meet the minimum temperature. The value 380.2 °C is predicted instead of 390.3 °C as for the V_{diffr} dependence on T. Concerning the whole experimental setup and span of the annealing temperatures used, we regard this difference as negligible keeping in mind the perfect linearity of the data. Moreover, the slope k' can be analysed in more detail using Eq. (**15**). The time integral can be estimated as the annealing temperature holding time of 1 h (thold = 3600 s). The specific surface energy is considered 2 J/m^2, according to the literature [**60**]. The molar volume can be calculated from the molar mass and density. The thickness of the boundary X can be estimated as 0.35 nm according to the unit cell parameters from the ICCD card. Hence the self-diffusivity may be determined.

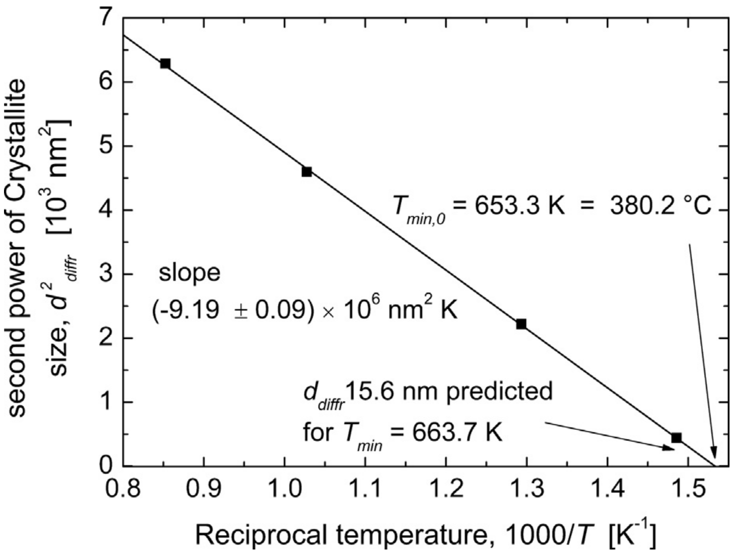

Fig. 9. The rate constant estimation for crystallite growth according to the Eq.

$$D_s = \frac{-k' R\lambda}{4\gamma V_{mol}} \cdot \frac{1}{t_{hold}} = 6.4 \times 10^{-16} cm^2 s^{-1} \qquad (18)$$

The value of 6.4 x 10^{-16} cm^{2}s^{-1} can be considered as the mean Ds estimation for the temperature range 670-1150 K and is in excellent agreement with the values known from the comprehensive reference of Erhart and Albe [**61**].

Since the diffusivity (Ds) exponentially depends on the temperature, it obeys the Arrhenius law with the activation energy Q contributing thus to the deviation of the strict linearity and the simplicity of the Eq. (**15**).

$$D_s(T) \propto e^{\frac{-Q}{RT}} \qquad (19)$$

Hence, the first 1/*T* dependence may be removed by multiplying with T together with the problem of the initial crystallite size similarly as in the grain case.

$$(d_{diffr}^{2} - d_{diffr0}^{2})T = -Tk't \tag{20}$$

Obtaining:

$$|Tk'| \propto e^{\frac{-Q}{RT}} \tag{21}$$

Hence, the Arrhenius plot for the additional 1/T dependence may be drawn.

$$\ln((d_{diffr}^{2} - d_{diffr}^{2}(400^{\circ}C))T) = -\frac{Q}{R}\cdot\frac{1}{T} + const \tag{22}$$

Finally, the activation energy Q for the D_s in Eq. (**18**) of the crystallite growth in **Fig. 10** was obtained as 31 kJ/mol, which is equivalent to 0.32 eV. This value is much smaller than the values of the migration barriers reported for the oxygen or zinc vacancy diffusion mechanisms; thus, the zinc interstitials are considered to be responsible for the observed crystallite growth [**62**]. Our estimated value is somewhat smaller than the 0.55 eV that was found by Thomas [**63**]. However, according to the more elaborated analysis and theoretical calculation of Erhart and Albe [**61**], there are several different mechanisms of the Zn interstitials diffusion possible. Among them, the energetic barrier of 0.32 eV can be associated with the interstitial in-plane mechanism and with the interstitial out-of-plane mechanism of the Zn diffusion in the ZnO lattice.

3.2. The correlation of the photocatalytic performance of the prepared ZnO nanostructured micro-lumps with their characteristics

The catalysts were prepared from the same precursor and always annealed for one hour in an air atmosphere. Because of the size of ZnO nanocrystallites ranges from ca 20 to 80 nm, no significant differences in their UV-vis diffusion reflectance spectra can be expected.

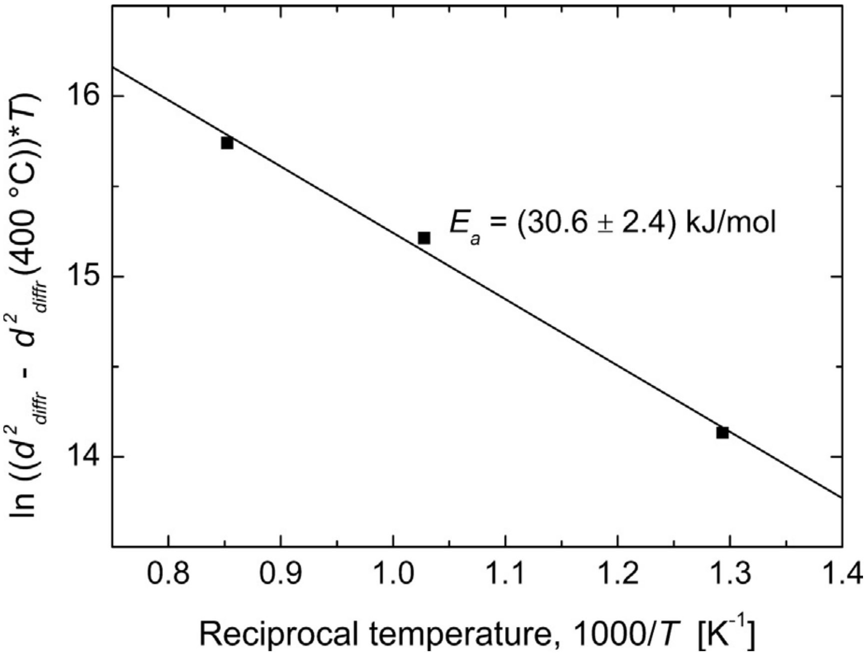

Fig. 10. The activation energy of the self-diffusion coefficient of ZnO nanocrystallite growth obtained from a linear plot of data according to the Eq. (**20**).

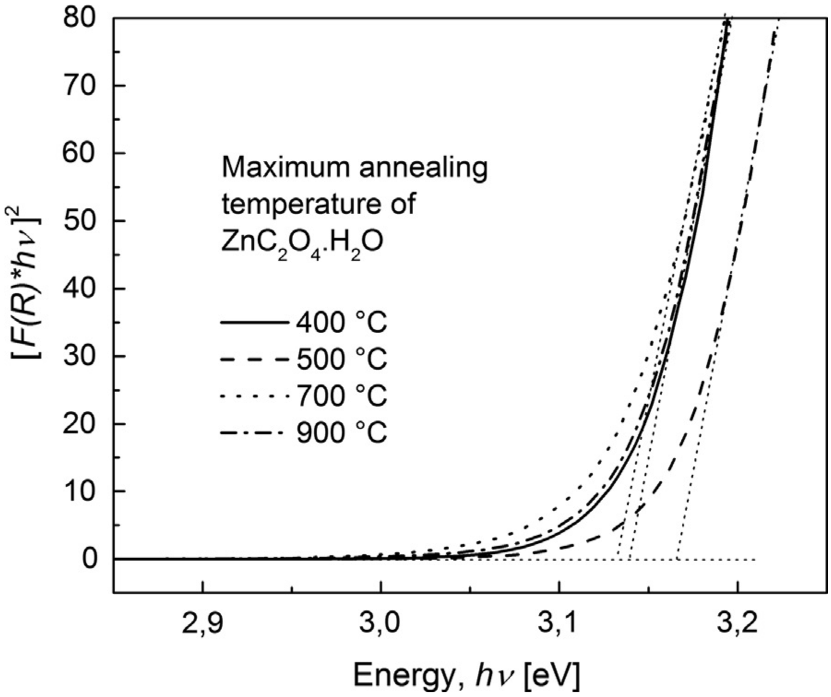

Fig. 11. Tauc plot for UV-Vis reflectance spectra collected on ZnO samples. The bandgap varies from 3.14 to 3.16 eV.

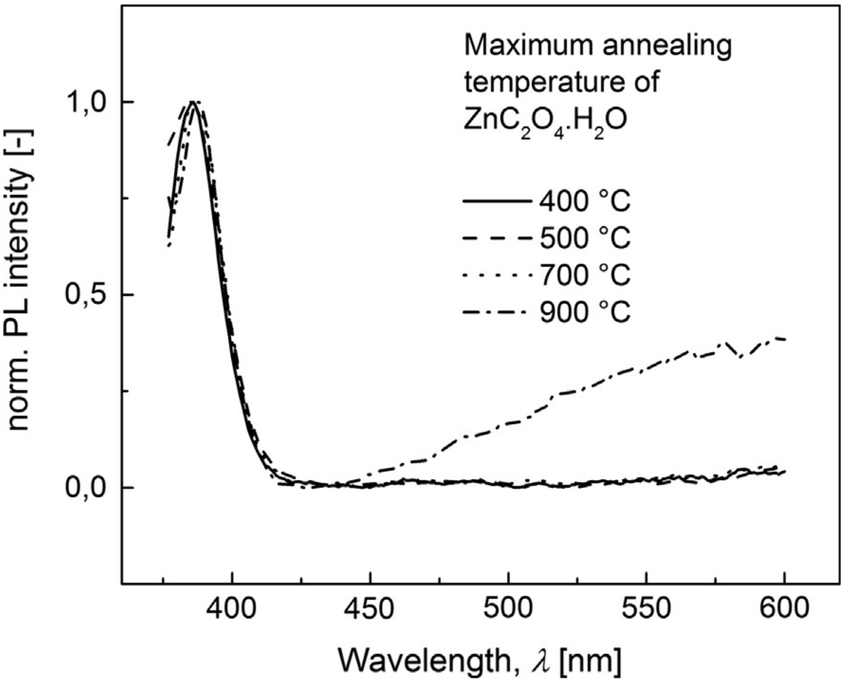

Fig. 12. The room temperature PL emission spectra of ZnO samples excited by a laser at Xexc = 332.2 nm.

The Tauc plot in Fig. 11 shows the absorption edges of the prepared samples. Indeed, the bandgap varies only from 3.14 to 3.16 eV and no significant tailing (i.e. the low concentration of deep states in the bandgap) is manifested too. Room temperature photoluminescence (RTPL) emission spectra plotted in **Fig. 12** show a strong emission peak at about 390 nm, which is assigned to near-bandgap exciton emission. Besides that, no other defect-related luminescence is manifested for the samples annealed at 400, 500, and 700 °C. Only one broad peak in the visible range with a maximum above the wavelength of 600 nm is present in the spectrum of the sample annealed at 900 °C. Its intensity is about one-third of the UV emission peak. Typically, green and yellow emissions are likely to defect emission due to various surface states, as explained by the vast majority of literature [**64-66**]. On the other hand, orange and red emissions are reported rarely and can be attributed to charge carriers trapped in deep states. These carriers tunnel and undergo radiative recombination. A broad distribution of these states may explain the broadness of the emission peak [**65,67,68**]. According to the spectroscopic analysis, we consider the electronic structure of the prepared materials to be similar enough, thus allowing to focus on the investigated effects. There are reports available confirming the similarity of the surface of ZnO prepared by annealing zinc oxalate in an air atmosphere to various moderate temperatures. On the other hand, high temperature, specific conditions, and annealing atmosphere settings and programmed changes are necessary to induce surface defects on ZnO nanoparticles and prepare different materials intentionally [**18,66,69-73**] According to the XRD analysis, no change in (1 0 0)/ (0 0 2) XRD peak intensity was observed. Therefore, the proportion of the polar faces to the surface of the crystallites remains the same for all samples, and the influence of exposure to different crystal faces can be excluded from further considerations [**54**]. Thus, it is expected that electronic structure and eventual volume and surface defect structure of prepared materials will be similar in all prepared samples, at least to such level, that specific manifestation of the hierarchical morphology levels should be the main factors, which contribute to the observed differences between the photocatalytic activity of these materials.

The discolouration of a dye solution under UV radiation was chosen as a method to demonstrate the photocatalytic effectiveness of our material system and to compare the efficiency of the prepared samples. It is widely used in the literature. The discolouration is the first step of photodegradation of the methyl violet 2B (MV) in the presence of the ZnO photocatalyst and was monitored by a UV-Vis spectroscopy. Any analysis of further products of the degradation process was not performed unlike advised in some other studies [**18,37**]. This approach was selected as a relatively fast and still relevant method for comparing the activity between the ZnO samples within one series differing in crystallite/aggregate size only. It was used with the full awareness of its disadvantage, which is its relatively low information depth as it allows measuring the initial stage of the process only and tells nothing about the mineralisation of the dye. This approach is considered sufficient for this study. **Fig. 13** exemplifies the obtained UV-Vis spectra for the system containing ZnO annealed at 500 °C. Here, the initial step of dye photodegradation is manifested by a decrease in the absorption maxima at 580 nm. **Fig. 14** shows the discolouration curves of the dye for all the ZnO samples prepared at various annealing temperatures. The ratio between the actual and the initial concentration is plotted against the time of the UV irradiation. As can be seen, the discolouration of the dye is accomplished within 120 min, and all curves obey pseudo-first-order reaction kinetics [**46**]. The rate constant was obtained from fitting this model into the data. The highest discolouration rate constant (see **Table 1**) was found for the sample annealed at 500 °C.

The photocatalysis is a complex process with at least several parameters influencing the final performance of the system. In our case, the mesoporous nanostructured lumps keeping the shape and size of the original precursor crystals floated due to the mechanical agitation in the solution of the substrate dye (MV) molecules. The system was irradiated from the top. The hierarchical morphology of the lumps of the photocatalyst was the variable in the experiment. All other conditions were kept the same. The photocatalytic discolouration mechanism was investigated with the aid of scavengers

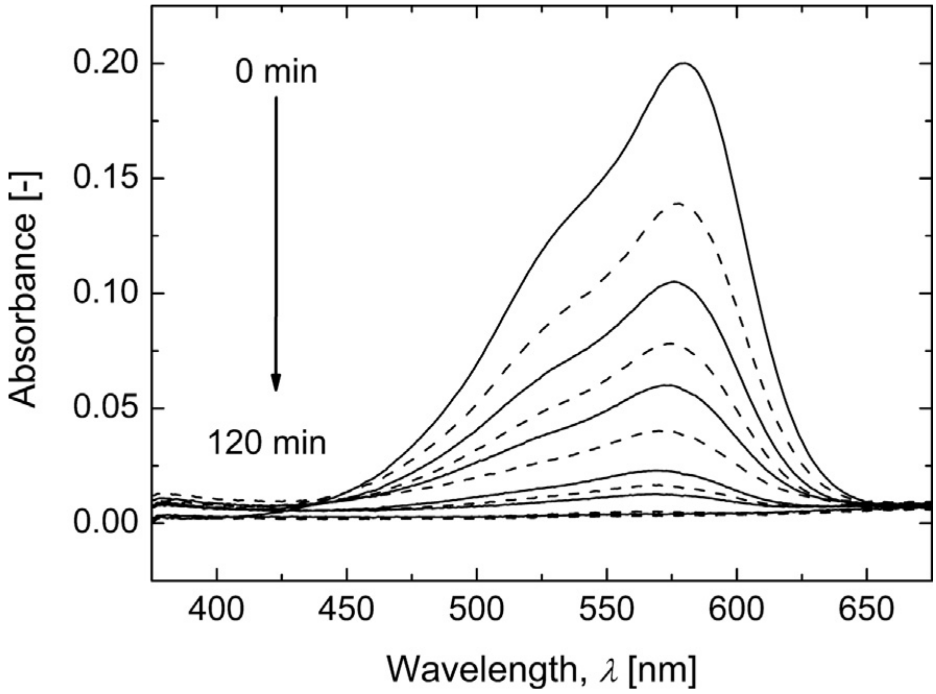

Fig. 13. The UV-Vis spectra of the methyl violet in the presence of the ZnO annealed at 500 °C. Note, that the last the three curves at the bottom of the graph overlap to a large extent.

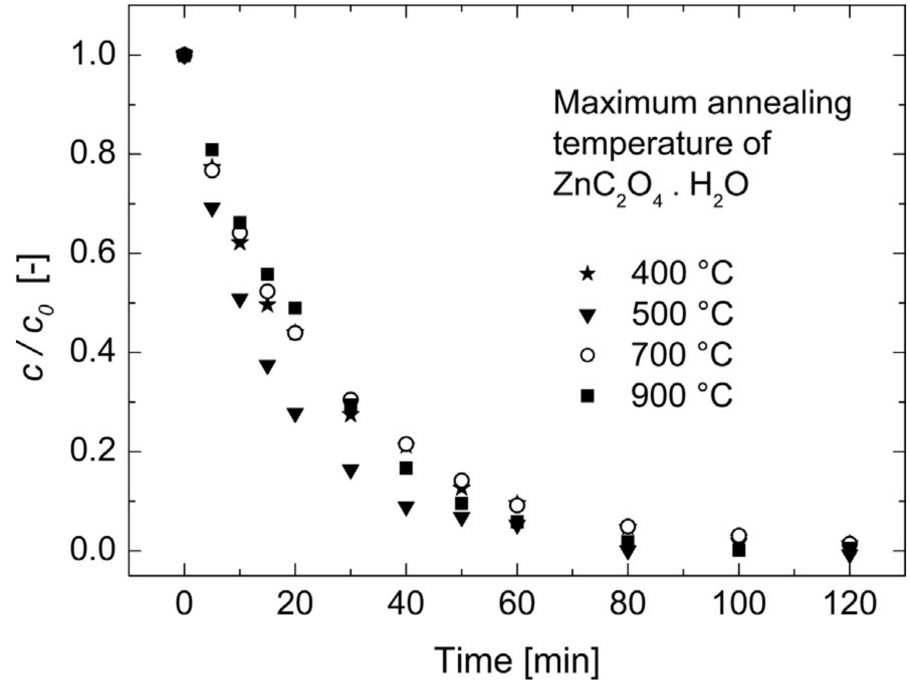

Fig. 14. The photocatalytic discolouration curves of the methyl violet as a function of time for the ZnO powders annealed at different temperatures.

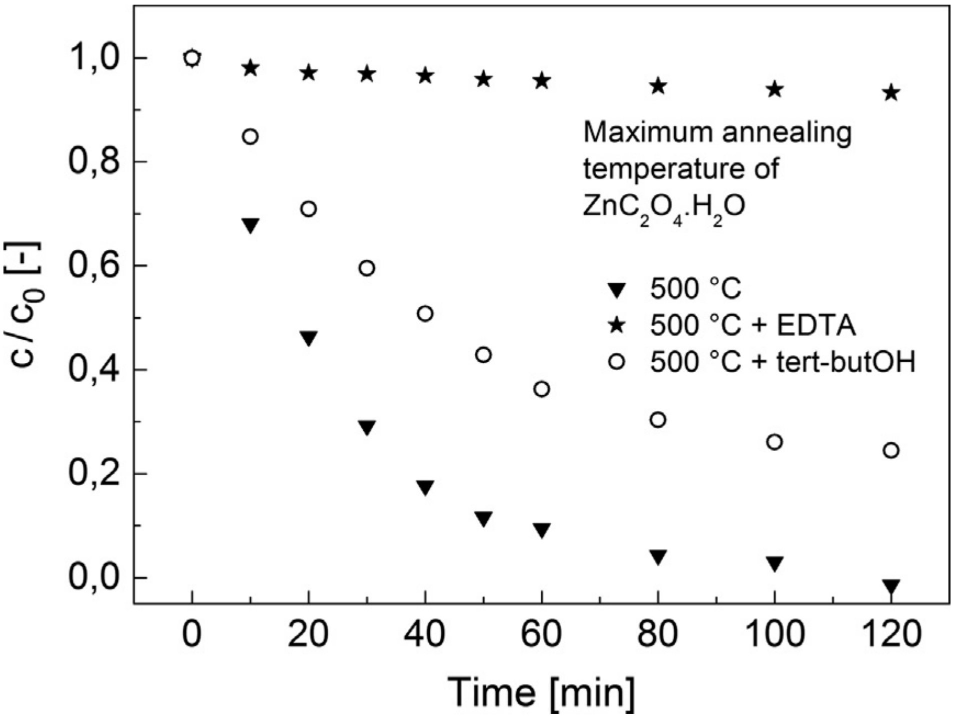

Fig. 15. The photocatalytic discolouration curves of the methyl violet as a function of time for the ZnO powder annealed at 500 °C in presence of scavengers. The curve recorded without scavengers is replotted from **Fig. 14** for comparison.

The discolouration experiment was repeated with the addition of EDTA and tert-butanol for the sample annealed at 500 °C. The results are shown in **Fig. 15**, where the discolouration curve without any scavenger is replotted for comparison too. It is evident, that EDTA as the hole scavenger kills the discolouration process, while the addition of hydroxyl radical scavenging tert-butanol slows the discolouration process only moderately.

A hole can interact with adsorbed hydroxide anion to produce OH radical, which subsequently reacts with the MV molecular cation in the solution, or the hole interacts directly with adsorbed dye molecular cation. On the other hand, an excited electron triggers a cascade of reactions. It can first reduce oxygen to a superoxide radical anion, which reacts with a proton to form a peroxide anion reacting then with another proton forming, thus hydrogen peroxide, which finally decomposes under UV light into two OH. All these species at any stage are highly reactive and can cause discolouration of the MV molecular cation [**40,74,75**]. Considering the observed result, the reaction pathway of holes oxidising adsorbed dye molecules is the favourable one. Thus, the dye adsorption seems to be the critical step in the discolouration mechanism.

The material prepared at 500 °C was selected as an example to verify the function of the catalyst. The catalyst was recollected after complete dispersion discolouration when the test was finished. The catalyst was left to settle and the supernatant was removed. The residue was dried naturally to the constant weight. A white powder of the same apperreance as the original catalyst was obtained. Some unavoidable weight losses were experienced due to manual procedure. Nevertheless, XRD analysis did not reveal any difference between the diffractograms recorded before and after the test. The diffractograms are shown in **Fig. 16**.

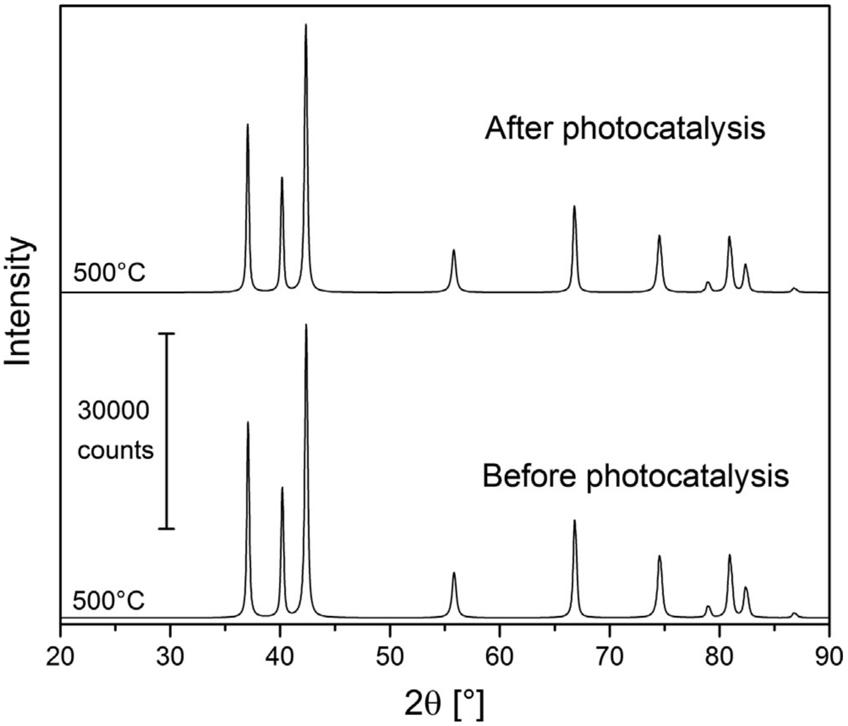

Fig. 16. Comparison of X-ray diffractograms recorded for the catalyst powder before and after testing.

As shown in **Fig. 14** and **Table 1**, the photocatalytic performance of our prepared materials has an optimum, which can be correlated with the trends of the morphological and the structural parameters.

Ohtani et al. [**23**] have proposed a basic model of the photocatalytic mechanism for particulate systems. According to their model, a photocatalyst should fulfil two requirements to attain a high photocatalytic activity. It has to have (i) a large surface area for absorption of the substrate molecules and to have (ii) high crystallinity to reduce the rate of futile electron-hole recombination. It means that the surface area and crystallinity mainly govern the photocatalytic activity of semiconductor oxides to a first approximation. However, these requirements work against each other, and a compromise is established [**48**]. The crystallinity of nanostructured systems increases at the expense of the specific surface area with increasing annealing temperatures.

In our case, the observed dependence of the photocatalytic performance of the prepared materials with an optimum for the material annealed at 500 °C cannot be merely the competition between the two primary factors (specific surface area and crystallite size). Since differences in the surface defect structure may be neglected in our study, three hierarchical levels of the catalyst's morphology and structure are considered to be the main factors involved in the non-monotonous dependence of the MV discolouration rate constant on the annealing temperature of the photocatalyst. Issues related to the mass transfer at the micrometre level, grain size-related phenomena, and eventual nanocrystallite size effects are discussed in the following paragraphs within a general structure-morphology interpretational framework corroborated by all our observations and obtained results.

3.2.1. The length scale of the micro-lumps and pores, i.e. micrometres

Dependence of the photocatalytic activity of a heterogeneous catalyst on its specific surface area is a generally accepted concept. However, the correlation between photocatalytic activity and the specific surface area of prepared catalysts is not straightforward for at least three reasons. First, the diffusion transport of MV molecules in and degradation products out of the pore labyrinth inside the lumps is limited. Thus, the core of the lump is not involved in the reaction, unlike in the systems with the hierarchical porous structure including macropores [**19-21**] as mentioned in the introduction. Second, the diffusion length of the active species such as superoxide, hydroxyl radicals is another factor limiting effectivity of the internal surface of the pores. Third, degradation UV light has most likely only a limited penetration depth into the lumps.

The BET surface area, the pore length, and the porosity (ϕ) of prepared materials depend monotonously on the sample annealing temperature while the observed discolouration rate constant dependence on the sample annealing temperature shows a maximum (see **Table 1** and **Fig. 17**). Some of these morphology linked factors contribute positively and some of them adversely to the performance of the photocatalyst.

The specific surface area is expected to contribute positively; nevertheless, a substantial part of the surface area cannot be accessible for the dye molecules. Note that the BET mean pore diameter (see **Table 1**) is only ca. three or four times bigger than the size of an MV molecule. Thus it represents a strongly impeding factor for diffusion. The charge of the internal surface of the pores may further decrease the hydrodynamic capillary diameter for the dye molecular cation MV^+. Nevertheless, the liquid medium is of moderate pH and ionic strength. The porosity was calculated from the total pore volume $V_{p\ BET}$ and the true density of ZnO and the values are shown in **Fig. 17**. The smaller ϕ is, the more it impedes diffusion. The length of the pores enormously increases with an increase in the BET surface area while the pore diameter almost does not vary with the BET surface area. The BET mean pore size, $d_{p\ BET}$, enabled the calculation of the BET total length of pores, $L_{p\ BET}$.

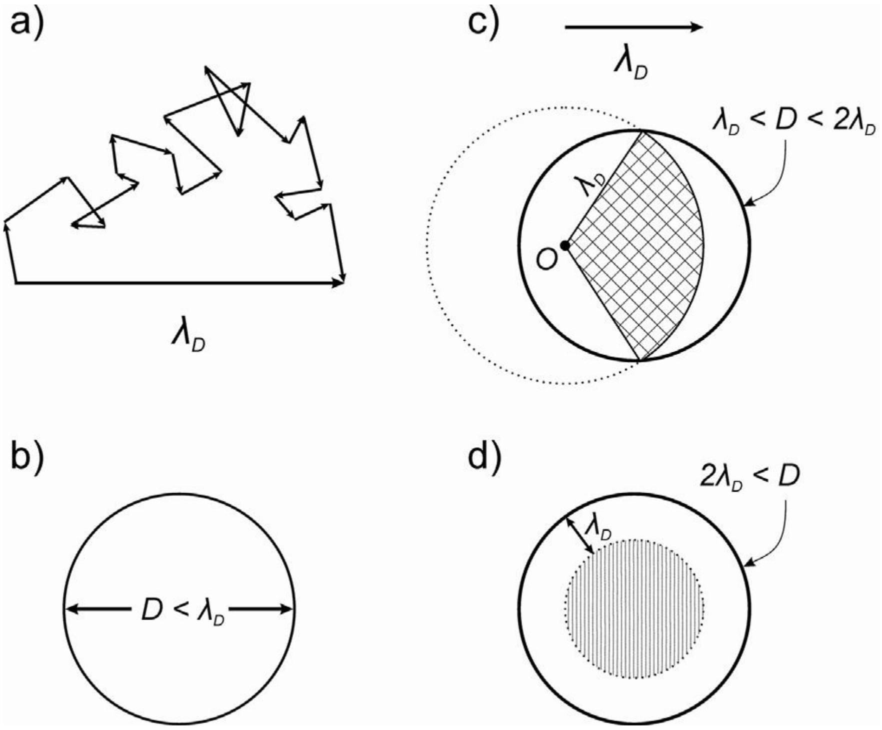

Fig. 18. A schematic illustration of the relationship between the average ex-citon diffusion length (XD, shown in the part a of the Figure) and the size of the ZnO particle in three cases b, c and d as discussed in the text.

This factor decreases with sample annealing temperature as plotted in **Fig. 17**. The bigger the value of this factor is, the less is the diffusion flow through the pores impeded.

The simple general pore flow geometric factor was analysed, since we have not enough data to evaluate tortuosity and constrictivity and there is a lack of reliable models in the literature for such low porosity regions of mesoporous systems [**76**]. However, both criteria (tortuosity and constrictivity) would work against the overall catalyst's performance and can be considered collinear with the general pore flow factor.

To summarise, the investigated morphological parameters act as both promoting and impeding on the photocatalytic activity of the prepared materials at the micrometre length scale. Therefore, it is possible to expect a maximum of the photocatalytic performance. Indeed, it was found in our case for the material annealed at 500 °C.

3.2.2. The length scale of the ZnO grains, i.e. Hundreds of nanometres

At the morphological level of a single grain, the exciton diffusion length may be the most critical factor controlling the photocatalytic performance. Only those excitons which come into contact with the surface exposed to the reaction medium can be involved in the reduction (electron) and the oxidation (hole) reactions. All other excitons end up in the futile electron-hole recombination. According to Noltemeyer et al. [**77**], the exciton diffusion length (H.D) in ZnO is about 110 nm at 300 K. Three possible scenarios are depicted schematically in Fig. 18. The exciton diffusion length (H.D) is its average travelling distance (**Fig. 18**a). All excitons can reach the surface if the particle diameter is smaller than the XD (**Fig. 18**b). In bigger particles, some excitons can recombine inside the volume of the particle due to travelling in the wrong direction. Such a situation is illustrated for an exciton created in point O in a particle of a diameter smaller than twice the length of XD in **Fig. 18**c. The third scenario is for a particle with the diameter bigger than twice the length of H.D. All excitons which are created deeper than the escape length XD can never reach the surface (**Fig. 18**d).

A continuous phase of the particle is assumed for identification of XD with a critical escape length for the exciton from a particle volume. In reality, the grains are composed of many nanocrystallites with interfaces between them. Such interfaces may serve as scattering centres or traps for excitons travelling through the grain volume and can obstruct the excitons created inside the grain volume to reach the grain surface. Scattering with the surface provides a path for the exciton to decay radiatively. On the other hand, trapping (i.e. strong carrier localization) of one of the charge carriers in a defect or surface state (trap states) is a fast process, which can efficiently compete with radiative recombination, resulting in the quenching of the exciton emission. Thus trapping makes the radiative recombination less likely and facilitates non-radiative relaxation by coupling to local vibrations [**78**]. Regardless of whether recombined by radiative or non-radiative decay path, such an exciton is inefficient in the photocatalytic process. The packing factor (1/F) expresses the ratio between the grain surface, which is exposed to its environment and the total surface area of nanocrystallites assembled into this grain. The value of 1/F factor decreases significantly with increasing the annealing temperatures (see **Fig. 5** again), indicating thus a decrease of the availability of the nanocrystallite surface for adsorption of the molecules. The role of the intercrystallite boundaries and the availability of a grain surface for photogenerated excitons is essential. Therefore, we calculated the portion of crystallites that have their surface at least partially exposed in the outer shell of the grain and the part of nanocrystallites buried in the inner core of the grain assuming a compact geometry of aggregation. It must be noted that the average size of single nanocrystallites is smaller than λ_D in all grains. The concept is illustrated in **Fig. 19**. When the number of nanocrystallites in the grain is lower than 13, all of them have direct access to the external space.

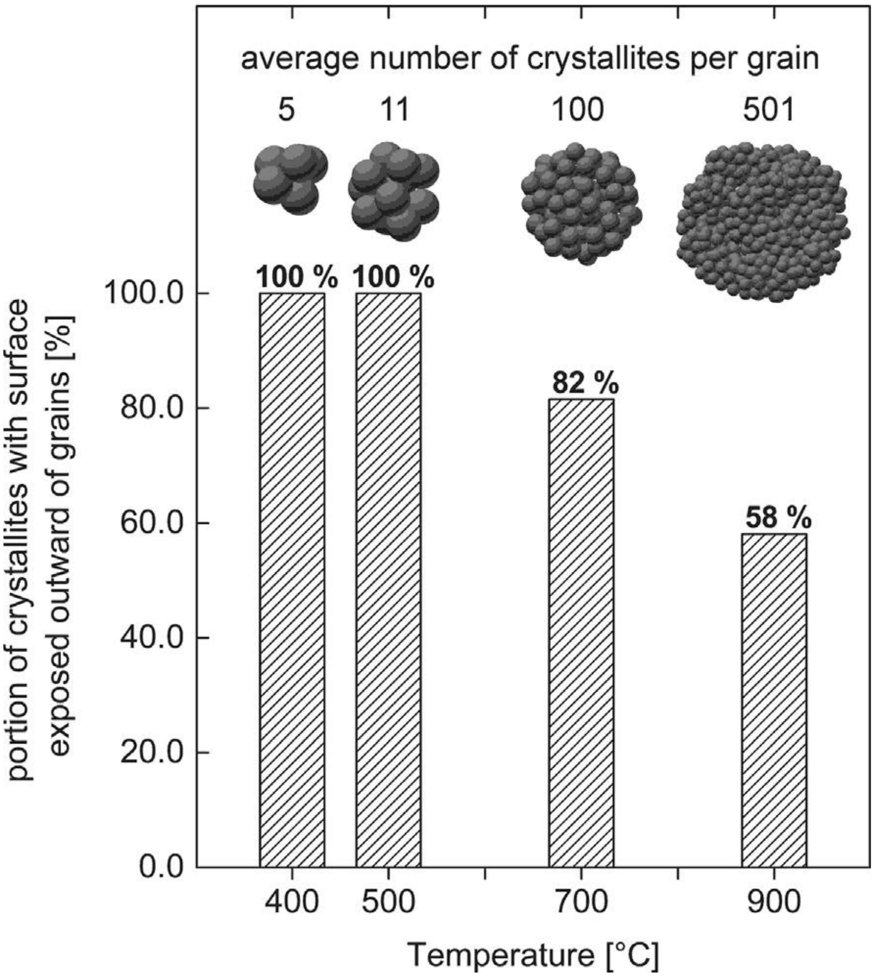

Fig. 19. The graph shows an estimation of the ratio of nanocrystallites buried in the volume of the aggregate and the number of nanocrystallites in the outer shell of the aggregate which have at least some part of their surface exposed to the surrounding environment. The ratio is expressed as a fraction of the surface exposed particles to the total number of particles in the grain. The estimation is based on the average grain size as obtained by the BET and the nanocrystallite size as obtained by the XRD. The geometrical considerations are illustrated by inserted schematic pictures.

Above this value, at least some particles will always be packed into a shell created by other particles. Hence it can be expected that the probability of futile electron/hole recombination event increases dramatically for materials obtained by calcination at temperatures higher than 500 °C.

3.2.3. The length scale of the ZnO crystallites, i.e. tens of nanometers

Single nanocrystallites can be considered as the smallest building blocks of the studied hierarchically structured material. Because of their size, which is in the tens of nanometers, it might be reasonable to examine quantum confinement effects. According to the original work of Bruse [**79**], the lowest excitonic state energy, i.e., band gap, depends on the size of the nanoparticle. However, the exciton Bohr radius α_0 is around 1.8 nm in ZnO, which is much smaller than the diameter of the nanocrystallites. Therefore, any strong or moderate quantum confinement effects are out of the discussion, and only weak confinement effects shall be considered further [**80-82**]. The interaction of light with ZnO nanoparticles can be distinguished into three different regions in reference to their size as determined by the radiative lifetime. First (i) nanoparticles smaller than the Bohr diameter of the exciton $2\alpha_0$, next (ii) nanoparticles bigger than $2\alpha_0$ but smaller than the wavelength of the incident light (360 nm in this case), and (iii) nanoparticles of a size comparable to the wavelength of the incident light [**80**]. The theoretical analyses showed that the rate of the radiative recombination decreases as the size increases in regions (i) and (iii), whereas it behaves oppositely in the region (ii) [**81,83-85**]. As the examined nanocrystallite sizes here fall into the region (ii) for all samples, it can be expected that the radiative recombination rate increases with a size increase. Since radiative recombination events are useless in the photocatalytic reaction, the increase of their rate must contribute negatively to the performance of the photocatalyst. Hence, the photocatalytic activity should decrease with increasing nanocrystallite size.

The last contribution to the photocatalytic performance, which remains to be examined is the efficiency of the light absorption since only absorbed photons of incident light can yield excitons. Hence, the dependence of intrinsic (nano)particle absorption with an increasing particle size must be analysed. The measurements available in the literature showed that intrinsic particle absorption increased with increasing size to the point at which the particles were essentially opaque. At larger sizes, the absorbance decreased with increasing size due to a decrease in the number of particles assuming a constant amount of the dispersed ZnO material. The particle size for optimum UV absorbance was found at about 40 nm. Reducing the particle size to less than 40 nm has a detrimental effect not only on the UV absorbance but also on the UVA/UVB absorbance ratio [**86**]. This value is in reasonable agreement with the work of Palmer et al. [**87**], who calculated an optimum particle size of 60 nm from refractive index measurements of the light scattering.

4. Conclusion

A series of nanostructured ZnO micro-lumps with mesoporous architecture was prepared by annealing zinc oxalate dihydrate precursor at four different temperatures in air. X-ray diffraction data and BET analysis provided a set of structural and morphological parameters that were confirmed by SEM. Exemplary correlated data were obtained. An extrapolation allowed for the identification of an initial temperature of 390 °C at which the nanocrystallite volume is theoretically zero and the process of ZnO nucleation starts. The TGA showed that the maximum precursor decomposition rate is attained at the same temperature. Similarly, it was estimated that aggregation of 4.5 nanocrystallites on average into one grain starts the grain growth process at this temperature.

The data were further analysed with the basic grain growth model. An agreement between the theory and the experiment was observed. The activation energy was estimated for the sintering process as well as for the ZnO nanocrystallite growth. The crystallite size was found to be linearly dependent on the reciprocal value of the thermodynamic temperature, which means that the growth was limited by the crystallite boundary mobility. The rate constant was analysed, and the value of the ZnO self-diffusion coefficient $D_s = 6.4 \times 10^{-16}$ cm^2s^{-1} was estimated, which is in agreement with the literature reported values. According to the refined analysis of the data, the activation energy of the self-diffusion coefficient $Q = 0.32$ eV was found, which allowed for identifying the mechanism of the crystallite growth in corroboration with the literature as the interstitial in-plane mechanism and the inter-stitialcy out-of-plane mechanism for the Zn diffusion in a ZnO lattice.

Prepared materials were tested in a standard test of photocatalytic activity based on an organic dye solution discolouration. The process followed pseudo-first order kinetics, and its rate constant was evaluated. Maximum activity was found for the material obtained by annealing at 500 °C. Furthermore, the reaction between h^+ and the dye adsorbed on the surface of the catalyst was identified as the key step in the mechanism of discolouration.

We developed an interpretational framework focused on contributions linked with the size scale levels of the hierarchical architecture of the prepared photocatalyst. Let the factors promoting the photocatalytic activity be denoted by a (+) sign and impeding factors by a (—) sign. There are various size scales associated with the corresponding hierarchical levels.

1. Although the size of the micro-lumps is in micrometres, their me-soporous morphology involves not only the length of the pores (macroscopic) but also their diameter (nm range) as representative physical length scales. Although the (BET) specific surface area (+) decreases monotonously, its availability for a photocatalytic reaction is controlled by geometrical constraints. The general pores flow geometric factor (+) decreases, while porosity (+) increases with the annealing temperature of the micro-lumps preparation; hence, these trends work against each other.
2. The ZnO micro-lumps are assembled from grains with a size scale mainly in the hundreds of nanometers. The effect of the particle size (—) is manifested for particles bigger than the escape length of the exciton (actually its diffusion length) which is about 110 nm in ZnO. Both scattering or trapping of an exciton on an internal interface between nanocrystallites aggregated into the grain discriminates the exciton from the photocatalytic process. This effect increases with increasing grain size as illustrated by the decrease in both the packing factor (+) and the fraction of crystallites in the outer grain shell (+) with the annealing temperature of micro-lumps preparation.
3. The size of individual nanocrystallites varies from ca 20 to 80 nm with applied annealing temperature. At this particle diameter length scale, the exciton radiation recombination rate (—) increases with the particle size, while intrinsic nanoparticle absorption (+) has a maximum for the particle diameter of about 40 nm.

To summarise the analysis of the photocatalytic activity of the ZnO hierarchically nanostructured mesoporous particles, we found that it is non-monotonously size-scale governed by a combination of effects contributing at various hierarchical levels of the particle morphology and thus tuneable by the annealing temperature used for the catalyst preparation.

References

[1] H. Morkoę, U. Ózgur, Zinc Oxide: Fundamentals, Materials and Device Technology, Wiley-VCH, Weinheim, 2009.

[2] C.C. Vidyasagar, Y.A. Naik, T.G. Venkatesh, R. Viswanatha, Solid-state synthesis and effect of temperature on optical properties of Cu-ZnO, Cu-CdO and CuO nanoparticles, Powder Technol.. 214 (2011) 337-343.

[3] M.F. Melendrez, et al., Growth of aligned ZnO nanorods on transparent electrodes by hybrid methods, J. Mater. Sci. 47 (2012) 2025-2032.

[4] Q. Zhang, C.S. Dandeneau, X. Zhou, G. Cao, ZnO Nanostructures for Dye-Sensitized Solar Cells, Adv. Mater. 21 (2009) 4087-4108.

[5] T. Shinagawa, S. Watase, M. Izaki, Size-controllable growth of vertical ZnO nanorod arrays by a Pd-catalyzed chemical solution process, Cryst. Growth Des. 11 (2011) 5533-5539.

[6] J. Zhang, et al., Hierarchically porous ZnO architectures for gas sensor application, Cryst. Growth Des. 9 (2009) 3532-3537.

[7] R.Y. Hong, et al., Synthesis, surface modification and photocatalytic property of ZnO nanoparticles, Powder Technol. 189 (2009) 426-432.

[8] M.B. Akin, M. Oner, Photodegradation of methylene blue with sphere-like ZnO particles prepared via aqueous solution, Ceram. Int. 39 (2013) 9759-9762.

[9] S. Rajappan-Achary, et al., Self-assembled zinc oxide quantum dots using spray pyrolysis methodology, Cryst. Growth Des. 11 (2011) 3790-3801.

[10] S. Guillemin, et al., Formation mechanisms of ZnO nanowires: the crucial role of crystal orientation and polarity, J. Phys. Chem. C 117 (2013) 20738-20745.

[11] P. Gu, X. Wang, T. Li, H. Yu, H. Meng, Solvothermal synthesis and growth mechanism of asymmetric ZnO hierarchical structures in diethylene glycol with ammonia solution, Cryst. Res. Technol. 48 (2013) 989-995.

[12] J. Yin, et al., Hierarchical ZnO nanorod-assembled hollow superstructures for catalytic and photoluminescence applications, Cryst. Growth Des. 10 (2010) 40-43.

[13] X. Li, et al., Comparison of photocatalytic activity of ZnO rod arrays with various diameter sizes and orientation, J. Alloys Compounds 580 (2013) 205-210.

[14] S. Bakand, A. Hayes, F. Dechsakulthorn, Nanoparticles: a review of particle toxicology following inhalation exposure, Inhal. Toxicol. 24 (2012) 125-135.

[15] M. Machovsky, I. Kuritka, P. Bazant, D. Vesela, P. Saha, Antibacterial performance of ZnO-based fillers with mesoscale structured morphology in model medical PVC composites, Mater. Sci. Eng. C-Mater. Biol. Appl. 41 (2014) 70-77.

[16] D. Vollath, Nanomaterials: An Introduction to Synthesis, Properties and Application, Wiley-VCH Verlag, Weinheim, 2008.

[17] M. Machovsky, I. Kuritka, J. Sedlak, M. Pastorek, Hexagonal ZnO porous plates prepared from microwave synthesized layered zinc hydroxide sulphate via thermal decomposition, Mater. Res. Bull. 48 (2013) 4002-4007.

[18] J. Zheng, et al., Shape-controlled fabrication of porous ZnO architectures and their photocatalytic properties, J. Solid State Chem. 182 (2009) 115-121.

[19] C.M.A. Parlett, K. Wilson, A.F. Lee, Hierarchical porous materials: catalytic applications, Chem. Soc. Rev. 42 (2013) 3876-3893.

[20] M. Sun, et al., Applications of hierarchically structured porous materials from energy storage and conversion, catalysis, photocatalysis, adsorption, separation, and sensing to biomedicine, Chem. Soc. Rev. 45 (2016) 3479-3563.

[21] X. Li, J. Yu, M. Jaroniec, Hierarchical photocatalysts, Chem. Soc. Rev. 45 (2016) 2603-2636.

[22] A.B. Djurisic, Y.H. Leung, A.M.C. Ng, Strategies for improving the efficiency of semiconductor metal oxide photocatalysis, Mater. Horizons 1 (2014) 400-410.

[23] B. Ohtani, Y. Ogawa, S. Nishimoto, Photocatalytic activity of amorphous-anatase mixture of titanium(IV) oxide particles suspended in aqueous solutions, J. Phys. Chem. B 101 (1997) 3746-3752.

[24] X. Li, et al., Engineering heterogeneous semiconductors for solar water splitting, J. Mater. Chem. A 3 (2015) 2485-2534.

[25] F. Amano, K. Nogami, B. Ohtani, Visible light-responsive bismuth tungstate photocatalysts: effects of hierarchical architecture on photocatalytic activity, J. Phys. Chem. C 113 (2009) 1536-1542.

[26] F. Amano, K. Nogami, M. Tanaka, B. Ohtani, Correlation between surface area and photocatalytic activity for acetaldehyde decomposition over bismuth tungstate particles with a hierarchical structure, Langmuir 26 (2010) 7174-7180.

[27] W. Cen, T. Xiong, C. Tang, S. Yuan, F. Dong, Effects of morphology and crystallinity on the photocatalytic activity of (BiO)(2)CO3 nano/microstructures, Ind. Eng. Chem. Res. 53 (2014) 15002-15011.

[28] D. Chen, J. Ye, Hierarchical WO3 hollow shells: Dendrite, sphere, dumbbell, and their photocatalytic properties, Adv. Funct. Mater. 18 (2008) 1922-1928.

[29] H. Chen, Y. Xu, D. Kuang, C. Su, Recent advances in hierarchical macroporous composite structures for photoelectric conversion, Energy Environ. Sci. 7 (2014) 3887-3901.

[30] B. Li, Y. Wang, Facile synthesis and enhanced photocatalytic performance of flowerlike ZnO hierarchical microstructures, J. Phys. Chem. C 114 (2010) 890-896.

[31] L. Zhu, M. Hong, G.W. Ho, Hierarchical assembly of SnO2/ZnO nanostructures for enhanced photocatalytic performance, Sci. Rep. 5 (2015) 11609.

[32] N. Audebrand, J.P. Auffredic, D. Louer, X-ray diffraction study of the early stages of the growth of nanoscale zinc oxide crystallites obtained from thermal decomposition of four precursors. General concepts on precursor-dependent microstructural properties, Chem. Mat. 10 (1998) 2450-2461.

[33] Z. Ha, L. Yue, Y. Zheng, Z. Xu, Rod-like zinc oxide constructed by nanoparticles: synthesis, characterization and optical properties, Mater. Chem. Phys. 107 (2008) 137-141.

[34] M. Muruganandham, I.S. Chen, J.J. Wu, Effect of temperature on the formation of macroporous ZnO bundles and its application in photocatalysis, J. Hazard. Mater. 172 (2009) 700-706.

[35] K. Intarasuwan, P. Amornpitoksuk, S. Suwanboon, P. Graidist, Photocatalytic dye degradation by ZnO nanoparticles prepared from X2C2O4 (X=H, Na and NH4) and the cytotoxicity of the treated dye solutions, Sep. Purif. Technol. 177 (2017) 304-312.

[36] R.M. German, Sintering theory and practice, Wiley, New York; Chichester, 1996.

[37] M. Kaneko, I. Okura, Photocatalysis: science and technology, Kodansha; Springer, Tokyo; Berlin; New York, 2002.

[38] A. Mills, An overview of the methylene blue ISO test for assessing the activities of photocatalytic films, Appl. Catal. B-Environ. 128 (2012) 144-149.

[39] Y. Tong, F. Cao, P. Tang, H. Chen, P.K. Chu, Photocatalytic behaviors of porous ZnO hierarchical structures fabricated via a precursor-pyrolyzing route, J. Mater. Sci. -Mater. Electron. 24 (2013) 89-95.

[40] H. Liu, et al., Synthesis of spherical Ag/ZnO heterostructural composites with excellent photocatalytic activity under visible light and UV irradiation, Appl. Surf. Sci. 355 (2015) 644-652.

[41] S.R. Morrison, T. Freund, Chemical role of holes and electrons in Zno photocatalysis, J. Chem. Phys. 47 (1967) 1543-&.

[42] B.E. Warren, X-ray diffraction, Dover Publications, New York, 1990.

[43] V. Uvarov, I. Popov, Metrological characterization of X-ray diffraction methods at different acquisition geometries for determination of crystallite size in nano-scale materials, Mater. Charact. 85 (2013) 111-123.

[44] Franęoise Rouquerol, Jean Rouquerol, K.S.W. Sing, Adsorption by powders and porous solids : principles, methodology and applications, Academic Press, San Diego, 1999.

[45] C. Hu, J. Mi, S. Shang, Ju. Shangguan, The study of thermal decomposition kinetics of zinc oxide formation from zinc oxalate dihydrate, J. Therm. Anal. Calorim. 115 (2014) 1119-1125.

[46] J. Kaur, S. Bansal, S. Singhal, Photocatalytic degradation of methyl orange using ZnO nanopowders synthesized via thermal decomposition of oxalate precursor method, Phys. B 416 (2013) 33-38.

[47] B.J. Zhang, S.A. Davis, S. Mann, Starch gel templating of spongelike macroporous silicalite monoliths and mesoporous films, Chem. Mat. 14 (2002) 1369-1375.

[48] Z. Jia, D. Ren, L. Xu, R. Zhu, Preparation, characterization and photocatalytic activity of porous zinc oxide superstructure, Mater. Sci. Semicond. Process. 15 (2012) 270-276.

[49] B. Małecka, E. Drożdż-Cieśla, A. Małecki, Mechanism and kinetics of thermal decomposition of zinc oxalate, Thermochim Acta 423 (2004) 13-18.

[50] S.S. Hayrapetyan, H.G. Khachatryan, The porosity of partly sintered nickel iron oxalates, Micropor. Mesopor. Mater. 89 (2006) 33-38.

[51] C. Shang, A. Barnabe, Structural study and phase transition investigation in a simple synthesis of porous architected-ZnO nanopowder, Mater. Charact. 86 (2013) 206-211.

[52] N. Jongen, H. Hofmann, P. Bowen, J. Lemaitre, Calcination and morphological evolution of cubic copper oxalate particles, J. Mater. Sci. Lett. 19 (2000) 1073-1075.

[53] H. Colfen, M. Antonietti, Mesocrystals: Inorganic superstructures made by highly parallel crystallization and controlled alignment, Angew. Chem. - Int. Edit. 44 (2005) 5576-5591.

[54] A. Mclaren, T. Valdes-Solis, G. Li, S.C. Tsang, Shape and size effects of ZnO nanocrystals on photocatalytic activity, J. Am. Chem. Soc. 131 (2009) 12540- + .

[55] J. Kadlcak, I. Kuritka, P. Konecny, R. Cermak, The effect of ZnO modification on rubber compound properties, GEMESED' 11 Proceedings of the 4th WSEAS international conference on Energy and development - environment - biomedicine, Corfu Island, Greece, 2011, pp. 347-352.

[56] V.D. Allred, S.R. Buxton, J.P. McBride, Characteristic properties of thorium oxide particles, J. Phys. Chem. 61 (1957) 117-120.

[57] P.A. Beck, J.C. Kremer, L.J. Demer, M.L. Holzworth, Grain growth in high-purity aluminum and in an aluminummagnesium alloy, Trans. Am. Instit. Mining Metallurg. Eng. 175 (1948) 372-400.

[58] J.E. Burke, Some factors affecting the rate of grain growth in metals, Trans. Am. Instit. Mining Metallurg. Eng. 180 (1949) 73-91.

[59] M.F. Yan, R.M. Cannon, H.K. Bowen, Grain-boundary migration. 1. Theory of impurity drag in ionic systems, Am. Ceram. Soc. Bull. 55 (1976) 397.

[60] S. Na, C. Park, First-Principles Study of the Surface Energy and the Atom Cohesion of Wurtzite ZnO and ZnS - Implications for Nanostructure Formation, J. Korean Phys. Soc. 56 (2010) 498-502.

[61] P. Erhart, K. Albe, Diffusion of zinc vacancies and interstitials in zinc oxide, Appl. Phys. Lett. 88 (2006) 201918.

[62] A. Janotti, Van de Walle, G. Chris, Fundamentals of zinc oxide as a semiconductor, Rep. Prog. Phys. 72 (2009) 126501.

[63] D.G. Thomas, Interstitial Zinc in Zinc Oxide, J. Phys. Chem. Solids 3 (1957) 229-237.

[64] P. Felbier, et al., Highly luminescent ZnO quantum dots made in a nonthermal plasma, Adv. Funct. Mater. 24 (2014) 1988-1993.

[65] U. Ozgur, et al., A comprehensive review of ZnO materials and devices, J. Appl. Phys. 98 (2005) 041301.

[66] P.S. Xu, Y.M. Sun, C.S. Shi, F.Q. Xu, H.B. Pan, The electronic structure and spectral properties of ZnO and its defects, Nucl. Instrum. Methods Phys. Res. Section B-Beam Interact. Mater. Atoms 199 (2003) 286-290.

[67] L. Spanhel, M.A. Anderson, Semiconductor clusters in the sol-gel process - quantized aggregation, gelation, and crystal-growth in concentrated Zno colloids, J. Am. Chem. Soc. 113 (1991) 2826-2833.

[68] Fan Hai-Bo, et al., Investigation of oxygen vacancy and interstitial oxygen defects in ZnO films by photoluminescence and x-ray photoelectron spectroscopy, Chin. Phys. Lett. 24 (2007) 2108-2111.

[69] A.B. Djurisic, Y.H. Leung, Optical properties of ZnO nanostructures, Small 2 (2006) 944-961.

[70] Y. Danhara, T. Hirai, Y. Harada, N. Ohno, Exciton luminescence of ZnO fine particles, Physica Status Solidi C - Current Topics Solid State Physics 3 (10) (2006) 3565- +.

[71] M. Fernandez-Garcia, J.A. Rodriguez, METAL OXIDE NANOPARTICLES; Sponsor Org.: Doe - Office Of Science, JOHN WILEY AND SONS, United States, 2007.

[72] L. Wang, et al., Systematic investigation on morphologies, forming mechanism, photocatalytic and photoluminescent properties of ZnO nanostructures constructed in ionic liquids, Inorg. Chem. 47 (2008) 1443-1452.

[73] Y. Lv, et al., Production of visible activity and UV performance enhancement of ZnO photocatalyst via vacuum deoxidation, Appl. Catal. B-Environ. 138 (2013) 26-32.

[74] A. Fujishima, X. Zhang, D.A. Tryk, TiO2 photocatalysis and related surface phenomena, Surf. Sci. Rep. 63 (2008) 515-582.

[75] Y. Nosaka, A.Y. Nosaka, Generation and detection of reactive oxygen species in photocatalysis, Chem. Rev. 117 (2017) 11302-11336.

[76] M. Matyka, A. Khalili, Z. Koza, Tortuosity-porosity relation in porous media flow, Phys. Rev. E 78 (2008) 026306.

[77] M. Noltemeyer, et al., Excitonic transport in ZnO, J. Mater. Res. 27 (2012) 2225-2231.

[78] R. Koole, E. Groeneveld, D. Vanmaekelbergh, A. Meijerink, M.D. de, Nanoparticles: Workhorses of Nanoscience, Springer Berlin Heidelberg, Berlin, Heidelberg, 2014, pp. 13-51.

[79] L.E. Brus, Electron electron and electron-hole interactions in small semiconductor crystallites - the size dependence of the lowest excited electronic state, J. Chem. Phys. 80 (1984) 4403-4409.

[80] B. Gil, A.V. Kavokin, Giant exciton-light coupling in ZnO quantum dots, Appl. Phys. Lett. 81 (2002) 748-750.

[81] B. Daudin, et al., Piezoelectric properties of GaN self-organized quantum dots, MRS Internet J. Nitride Semicond. Res. 4 (1999) art. no.-G9.2.

[82] A.D. Andreev, E.P. O'Reilly, Optical transitions and radiative lifetime in GaN/AlN self-organized quantum dots, Appl. Phys. Lett. 79 (2001) 521-523.

[83] A.V. Kavokin, Exciton oscillator strength in quantum-wells - from localized to free resonant states, Phys. Rev. B 50 (1994) 8000-8003.

[84] D.J. Norris, A.L. Efros, M. Rosen, M.G. Bawendi, Size dependence of exciton fine structure in CdSe quantum dots, Phys. Rev. B 53 (1996) 16347-16354.

[85] S.S. Hong, T. Joo, W.I. Park, Y.H. Jun, G.C. Yi, Time-resolved photoluminescence of the size-controlled ZnO nanorods, Appl. Phys. Lett. 83 (2003) 4157-4159.

[86] E.G. Goh, X. Xu, P.G. McCormick, Effect of particle size on the UV absorbance of zinc oxide nanoparticles, Scr. Mater. 78-79 (2014) 49-52.

[87] P. Stamatakis, B.R. Palmer, G.C. Salzman, C.F. Bohren, T.B. Allen, Optimum particle-size of titanium-dioxide and zinc-oxide for attenuation of ultraviolet-radiation, J. Coat. Technol. 62 (1990) 95-98.